Rapid multiexposure *in vivo* brain imaging system using vertical cavity surface emitting lasers as a light source

Yaaseen Atchia,[1,2] Hart Levy,[1,2] Suzie Dufour,[1,2] and Ofer Levi[1,2,*]

[1]The Edward S. Rogers Sr. Department of Electrical and Computer Engineering, University of Toronto, 10 King's College Road, Toronto, Ontario M5S 3G4, Canada

[2]Institute of Biomaterials and Biomedical Engineering, University of Toronto, 164 College Street, Toronto, Ontario M5S 3G9, Canada

*Corresponding author: ofer.levi@utoronto.ca

We demonstrate an imaging technique implementing vertical cavity lasers with extremely low transient times for a greatly simplified realization of a multiexposure laser speckle contrast imaging system. Data from multiexposure laser speckle imaging was observed to more closely agree with absolute velocity measurements using time of flight technique, when compared to long-exposure laser speckle imaging. Furthermore, additional depth information of the vasculature morphology was inferred by accounting for the change in the static scattering from tissue above vessels with respect to the total scattering from blood flow and tissue. © 2013 Optical Society of America

OCIS codes: 110.6150, 030.6140, 170.3880.

1. Introduction

Wide-field brain optical imaging techniques have garnered much attention in recent years due to their non-invasive nature and high spatiotemporal resolution [1–4]. Hemodynamic monitoring of neural activity has been demonstrated through several wide-field optical imaging methods, providing measurements which show strong correlation with more invasive techniques such as electrode electrophysiology measurements [5]. The simultaneous implementation of two commonly used optical techniques, intrinsic optical signal imaging (IOSI) and laser speckle contrast imaging (LSCI), can provide concurrent data on relative blood oxygenation levels and flow velocities. Optical biomedical imaging techniques also give an advantage over nonoptical modalities such as functional magnetic resonance imaging, positron emission tomography, and computed tomography [6], due to their simple design, low cost, and potential of miniaturization for portable imaging [7,8].

LSCI is an optical technique capable of producing maps of relative blood velocity *in vivo* through the interference of coherent light [9]. A speckle pattern is produced from multiple scattering events of the coherent light, resulting in a random interference pattern on the detector. Dynamic scatterers, in the form of moving blood cells, induce phase shifts in the scattered light, causing changes in the speckle pattern. A quantitative statistical value associated with the speckle pattern is called the spatial speckle contrast ratio, K, defined as the ratio of the spatial standard deviation, σ, and mean intensity, $\langle I \rangle$, in a selected window around the pixel [10,11]:

$$K = \frac{\sigma}{\langle I \rangle}. \tag{1}$$

This ratio, K, can be shown to have dependence on the velocity of the dynamic scatterers. The autocorrelation

function of the electric field, $g_1(\tau)$, exhibits an exponential decay with a characteristic time, τ_c, which is inversely proportional to blood flow velocity v. The relationship between K and τ_c depends on whether the velocity distribution of scatterers is assumed to be either Gaussian or Lorentzian. In the "long-exposure" approximation, where camera exposure time T is much larger than τ_c, both Gaussian and Lorentzian velocity distribution models reduce to the same relation between K and τ_c [12], namely:

$$\tau_c = 2TK^2. \tag{2}$$

Equation (2) can be used to produce a wide-field relative blood flow velocity map by directly squaring the reciprocal of the K map obtained from a single, long-exposure time image. This "long-exposure" approximation does not account for the influence of static scatterers located above and below the blood vessels on the speckle contrast ratio, causing deviations in K and in the computed quantitative flow velocity map. Parthasarathy $et\ al.$ derived a multiexposure model for LSCI based on a Lorentzian velocity distribution of scatterers [13], which provides an improved flow interpretation by accounting for static scatterers. In this model, the contrast ratio K is given as follows:

$$K(T,\tau_c) = \left(\beta\rho^2 \frac{e^{-2x}-1+2x}{2x^2} + 4\beta\rho(1-\rho) \frac{e^{-x}-1+x}{x^2} \right.$$
$$\left. + \nu_{\text{ne}} + \nu_{\text{noise}} \right)^{\frac{1}{2}}, \tag{3}$$

where $x = T/\tau_c$, $\rho = I_f/(I_f + I_s)$ is the fraction of light that is dynamically scattered, I_f is the contribution from dynamic scatterers, and I_s is the contribution from static scatterers, β is a normalization factor, ν_{ne} is a variance term associated with non-Ergodic light, and ν_{noise} is the experimental noise, mainly coming from the detector. The accuracy of Eq. (3) is limited, since the assumption of Lorentzian scatterer velocity distribution does not always hold. Furthermore, multiple exposures are needed to fit all parameters, and the fitting process is computationally intensive. In many cases, to simplify the fitting, it is possible to apply a short exposure time limit, $\lim_{x\to0} K = \sqrt{\beta + \nu_{\text{noise}}}$. In this limit it is assumed that the noise becomes equivalent to the sum of the static speckle pattern (from tissue or bone) and the camera noise. As x approaches zero, the first three terms of the Taylor expansion of the exponential in Eq. (3) give

$$\lim_{x\to0} K = \sqrt{\beta + \nu_{\text{noise}}} = \sqrt{\beta\rho(2-\rho) + \nu_{\text{ne}} + \nu_{\text{noise}}}. \tag{4}$$

Thus, we find that $\nu_{\text{ne}} = \beta(1-\rho)^2$ and we are able to remove one fitting parameter in Eq. (3). On the other hand, assuming Gaussian velocity distribution of scatterers [14], the following relation is derived:

$$K(T,\tau_c) = \left(\beta\rho^2 \frac{e^{-2x^2}-1+\sqrt{2\pi}\,\text{xerf}\left(\sqrt{2}x\right)}{2x^2} \right.$$
$$+ 2\beta\rho(1-\rho) \frac{e^{-x^2}-1+\sqrt{\pi}\,\text{xerf}(x)}{x^2}$$
$$\left. + \beta(1-\rho)^2 + \nu_{\text{noise}} \right)^{\frac{1}{2}}. \tag{5}$$

Equations (3) and (5) can be used to estimate relative velocity maps from multiexposure imaging, using a Lorentzian or Gaussian model, respectively. This can be particularly useful to minimize trauma during chronic surgery using thinned skull [14], which requires taking into account the contribution of static scatterers for accurate hemodynamic quantitative measurements.

Relative flow maps obtained using each of the two multiexposure models, as well as from long-exposure imaging, can be compared to time of flight (TOF) measurements. A green LED can be used as a separate illumination source to measure absolute flow velocities $in\ vivo$ by direct erythrocyte tracking, taking advantage of the greater absorbance of red blood cells at these wavelengths to measure blood cell movement [15]. By examining a rapid succession of image frames, erythrocyte velocities can be measured based on the distance traversed and the time between frames. However, this technique requires extremely high frame rates, in excess of 100 frames per second (fps), to allow tracking of physiologically relevant speeds [15]. For high flow speeds (10 mm/s) a lower frame rate would result in overwhelming uncertainties in velocity measurements.

Acquiring multiple exposures continuously usually requires a complex optical setup due to the wide range of exposures needed. Most laser sources provide single mode illumination only over a narrow range of optical powers, requiring costly acousto-optic modulators for controlling the exposure time and intensity in each acquired frame [13,14]. The long exposure times required leads to sensor saturation without extra optical components. Vertical cavity surface emitting lasers (VCSELs) are an attractive light source for this imaging application because of their low cost and power efficiency [16]. They can easily be adapted to provide a range of pulse times during a fixed camera exposure time due to their rapid power stabilization time (<10 μs).

In this paper, we show a novel imaging technique using VCSELs with extremely low transient times for a greatly simplified realization of a multiexposure imaging system. We used VCSELs for multi- and long-exposure LSCI measurements to map vascular velocities and compare these estimates to TOF measurements obtained using a green LED. Using our implementation, we account for errors induced by the presence of static scatterers, and compare results between multi- and single-exposure techniques.

We also investigate the differences between the Gaussian and Lorentzian multiexposure models as compared with absolute velocities obtained by TOF measurements. As multiexposure analysis requires curve-fitting steps, errors due to camera lens defocusing in the long-exposure and multiexposure models under Gaussian/Lorentzian scatter distribution assumptions are also considered. Finally, using the multiexposure model parameter ρ, relative depth information is estimated to produce three dimensional vasculature maps.

2. Methods

A. Imaging System

Raw images are obtained using a 14 bit CCD camera, QImaging Rolera EMC2, with pixel size of 8 µm. This camera was operated at its maximum frame rate of ~33 fps with 500 × 500 pixels. As long exposure times are required for accurate parameter fitting in multiexposure imaging, the frame rate was limited by exposure time, T. The camera triggers a laser by sending an output pulse to a current source (Keithley 6221), allowing for accurate current and timing coordination of the laser illumination as shown in Fig. 1(a).

This system was used to illuminate the exposed cortex of rodent subjects. The cortex was imaged through two back-to-back lenses (Nikon, $F = 28$ mm and $F = 50$ mm, $F/2$) providing a 1.8× magnification. The camera and lenses are mounted on a vertical translation stage and controlled by a micrometer screw, allowing small adjustments of the focal plane.

A 680 nm Vixar Inc. VCSEL was used as an illumination source for speckle imaging, providing approximately 1 mW of optical power. The device was powered through a low-noise Keithley 6221 current source at currents ranging from 1.05 to 3.0 mA, providing single-mode illumination adequate for speckle imaging [Fig. 1(c)]. A chosen sequence of exposures pulse times was preprogrammed to the current source, using the camera trigger as a master timer for the system. The sequence was coded in Mathworks MATLAB and sent to the current source through a general purpose interface bus (GPIB) interface. As shown in Fig. 1(b), the VCSEL illumination was initiated 300 µs before camera exposure time onset to ensure that laser transient time (<10 µs) has a minimal effect on captured frame intensity. The system was tested using a brain tissue phantom comprised of a silicone disc and titanium dioxide particles. This mixture effectively provides a scattering coefficient similar to values found in rat cortex.

The multiexposure frames range from 50 µs to 30 ms exposure time while long exposure frames were taken at 6 ms. The multiexposure sequence produces a 600× dynamic range in exposure times. The CCD camera has a linear full well of 32,700e− with read noise of 20e−. Assuming that long-exposure images have an average of 80% of
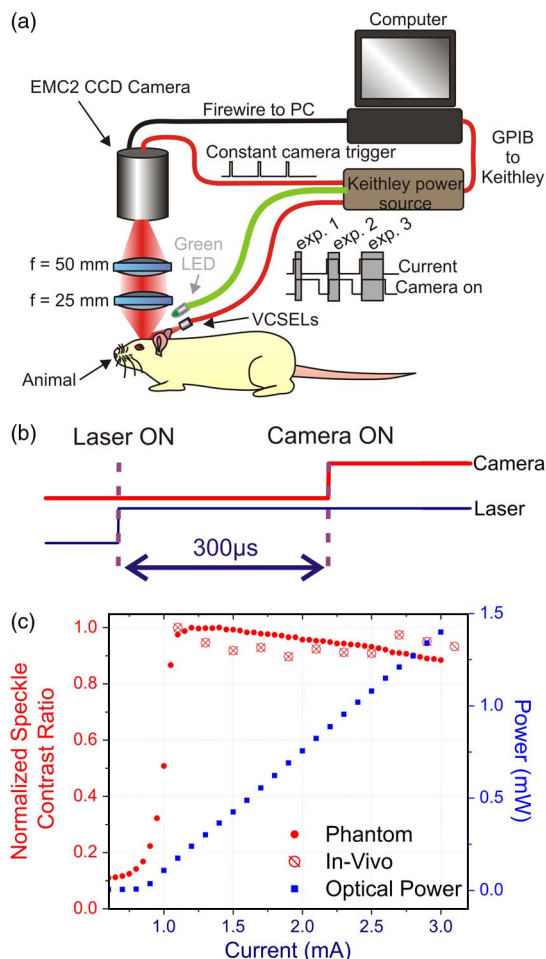

Fig. 1. (Color online) (a) Experimental setup of the imaging system. (b) Camera and laser onset time schematic; the VCSEL illumination was initiated 300 µs (much greater time than laser transient time) before the camera exposure time onset, and (c) changes of speckle contrast ratio with current on phantom (red dots) and *in vivo* (red crossed circle) and changes of optical power with current (blue squares). Note that K values do not change more than 15%, from 1.05 to 3.0 mA, while providing 7-fold increase in optical power.

the full well (i.e., ~26,000e−, which will minimize saturated pixels) and low exposures are imaged at 15 times the read noise, 300e−, we can obtain acceptable images using constant illumination over an 86-fold changes in exposure time. As a 600× range was desired, the source current can be adjusted to provide more optical power, as long as the laser spatial mode is largely single mode and static speckle contrast ratio does not vary. From Fig. 1(c), we find that speckle contrast ratio does not change more than 15% within the 1.05–3 mA range, indicating that the laser is largely single mode and laser coherence is only slightly affected. Differences in the trend between phantom and *in vivo* arise from small movements of the animal due to breathing and heartbeat. In this current range, optical power changes by a factor of 7 which, when multiplied with the dynamic range of the camera (86×), allowed slightly above the 600× range of exposures required.

Green illumination was used for TOF measurements as discussed in the introduction. The illumination source was a green LED (Green Batwing, Luxeon Star/O, Philips Lumileds) operating at ~525 nm with a supply current of 100 mA (Keithley 6221 power supply) providing approximately 25 mW of optical power. Since making TOF measurements requires fast frame rates, the image size was reduced to 200×200 pixels at exposure times of 1 ms, allowing a maximum frame rate of 118 fps. Several regions of interest (ROIs) were evaluated to compare with the full-frame images of speckle maps.

B. Animal Preparation for *in vivo* Surgery

Animal preparation was completed according to procedures outlined in our previous studies [4]. All animal studies were performed in accordance with ethics protocols approved by the University of Toronto Animal Care Committee. Animal surgery was done on male Sprague Dawley rats (weight 150–250 g). Prior to surgical procedures, anesthesia was induced using 5% isofluorane. During surgery and imaging, anesthetic levels were reduced to 2%–3% mixed with oxygen flowing at a rate of 1 liter/min. The animal was placed in a stereotaxic mount and body temperature was maintained at 37 °C using a thermal blanket (T/Pump, Gaymar Industries). Craniotomies with diameters of approximately 4 mm were performed on the right and/or left hemisphere between bregma and lambda ridges, and the dura mater was removed in the exposed region. Agarose gel was applied to the exposed brain surface, and was kept inside a petroleum jelly wall and covered with a glass cover slip to create a flat imaging plane.

C. Image Analysis

Image processing was performed using MATLAB and ImageJ software packages. Images from the camera were sorted using MATLAB based on changes in gray levels between each exposure. Speckle contrast ratio values, K were computed in ImageJ using a 5×5 pixel window around each pixel to find the ratio of standard deviation and mean [Eq. (1)]. Statistical variation in speckle contrast ratio values was reduced by taking the average over 300 contrast images. The resulting speckle contrast ratio maps were fitted to Eqs. (3) and (5) by similar methods as in [13] and [14], providing relative velocity maps for the multiexposure models. Equation (2) was used to obtain long-exposure relative velocity maps.

3. Results

Speckle contrast ratio images are limited by static scatterers above and below vessels. To account for these errors, a multiexposure approach has been adopted using inexpensive and nonmoving parts. We anticipate a better agreement in comparing multiexposure laser speckle to absolute velocity by doing TOF measurements as opposed to long exposure. The estimate of the amount of static scatterers can also

be used to obtain information about morphology of the vasculature.

A. VCSELs as Light Sources for Multiexposure

Multiexposure results obtained using VCSELs are shown in Fig. 2. Exposure time ranges from 50 µs to 30 ms with the higher exposure limiting the camera frame rate to ~33 *fps*. Fig. 2(a) shows speckle contrast ratio data obtained at each exposure averaged over 300 LSCI images through our technique of changing current. As LSCI is a wide-field technique, a large number of vessels are available for analysis. As predicted by theory, increasing the exposure time reduces the value of speckle contrast ratio [13,14]. Figure 2(b) shows the changes in speckle contrast ratio with increasing exposure time in a
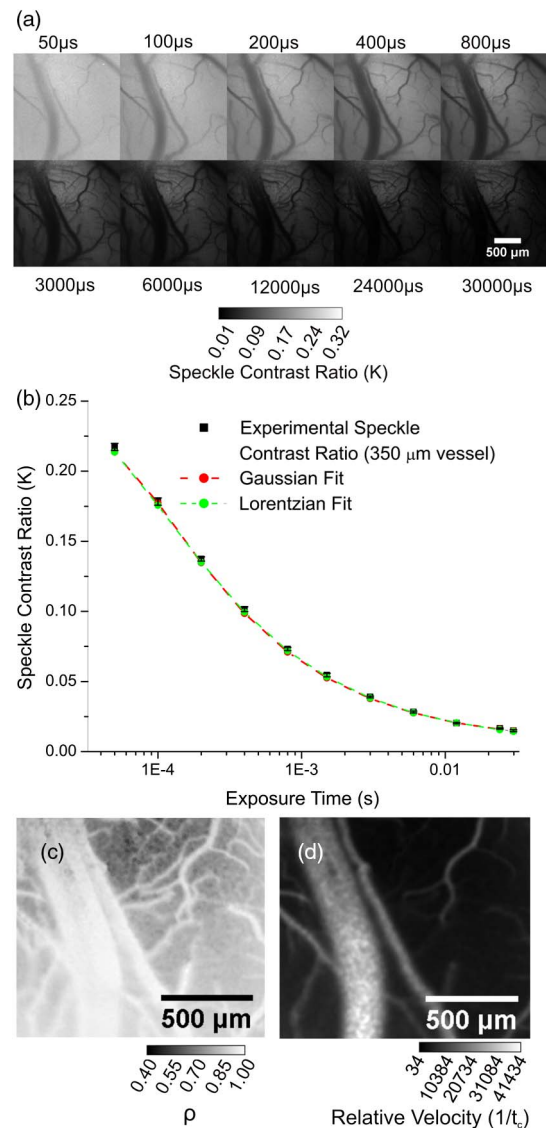

Fig. 2. (Color online) (a) 300 averaged speckle contrast ratio map from 50 µs to 30 ms obtained by changing exposure time of VCSELs. (b) Speckle contrast ratio data from a vein fitted to both a Gaussian and Lorentzian model. (c) ρ map obtained from VCSELs. (d) Relative velocity map obtained using VCSELs.

large vessel. The data is fit to both Gaussian [Eq. (5)] and Lorenztian [Eq. (3)] models. The two important parameters obtained from multiexposure fitting were ρ, being the ratio of dynamic to total scatters, and $1/\tau_c$, a parameter proportional to velocity, which are shown in Figs. 2(c) and 2(d), respectively. We find ρ to be larger in vessels, while parenchyma values were much lower, in agreement with what is expected. Multi-exposure measurements were also performed using neutral density filters to control optical power output, while maintaining a constant current. With these measurements we found no significant changes in ρ and a minimal change in relative velocity esti-mates $(4.0 \pm 2.8\%)$.

B. Accounting for Deviations due to Static Scatterers

Since speckle imaging is only able to provide mea-surements of relative flow velocities, a comparison to absolute speed measurements is needed to verify and compare results between models. With red blood cells being 5–9 μm and a pixel size of 4 μm after mag-nification, accurate TOF measurements require a high frame rate. As such, smaller ROIs of 200×200 are used to obtain a constant 118 fps, which is adequate to cover the range of velocities found in both veins and arteries. Comparing both the long and multiexposure approaches of speckle imaging to erythrocyte tracking, we can garner information on where each technique prevails. Figure 3 shows the comparison of relative velocities from speckle maps to absolute velocities for the long exposure and Lorentzian/Gaussian multiexposure models. There is an observed large deviation between the absolute velocities and the velocities predicted by the long-exposure model, mainly in vessels of high velocity. This observation is well understood by plotting the speckle equations [17]. This error is further accentu-ated by the strong presence of static scatterers (low ρ values). Using a multiexposure approach allows correcting for the error due to static scatterers and improves the correlation between speckle imaging and absolute velocities obtained via a TOF

technique. This correlation increase has been con-firmed in five different regions within the cortex. No significant differences between Gaussian and Lorentzian fits were found during those attempts. This is due to the wide distribution of vessel sizes and velocities present in this wide-field imaging technique. It is known that using a Lorentzian ap-proximation of the distribution of scatterers better suits vessels with Brownian motion while a Gaussian is better for inhomogeneous motion [18]. However, as speckle contrast ratio gives a relative velocity map, several vessels were needed to compare to the abso-lute velocities obtained from a green TOF technique. When comparing vessels of different sizes, it is not possible to estimate the advantage of using either distribution. Gaussian or Lorentzian distributions for multiexposure measurements can be used inter-changeably to provide more accurate flow measure-ments compared to a single long-exposure frame.

C. Errors due to Defocusing

When imaging complex vasculature such as vessels in the brain, maps will contain features outside the focal plane. It is important to know how accurate measurements of these features are compared with the best focused image. Comparing the ρ map from Gaussian and Lorentzian models from focal depths of −200 to +600 μm as compared to best focus in in-crements of 100 μm, it is found that ρ values do not change more than 20% [Figs. 4(a) and 4(b)]. On the other hand, relative velocity maps suffer more from changes in the imaging plane, with values varying up to 80% in vessels [Figs. 4(c)–4(e)]. This suggests ac-curate values of ρ can be obtained even if the camera focal plane is not ideal. On the other hand, relative velocity values are as prone to depth variation in both the long- and multiexposure regimes. We can conclude that accounting for static scatterers does not lead to improved depth of field in the measure-ment of velocity. It is also apparent that small vessels have the greatest errors in both ρ and relative veloc-ity maps. This observation is in agreement with a general modulation transfer function curve shape,
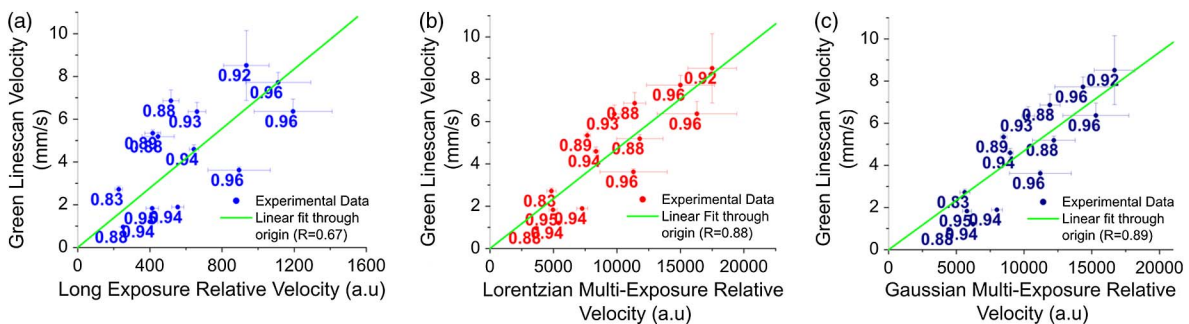

Fig. 3. (Color online) (a) Comparison of long-exposure relative velocity map to absolute velocities obtained using a green LED. ρ values are shown on each point. A linear fit through the origin is in green. (b) Comparison of a Lorentzian multiexposure speckle imaging to absolute velocities. Significant improvement in a linear fit through the origin is found as compared to using the long-exposure approx-imation. (c) Comparison of a Gaussian multiexposure speckle imaging to absolute velocities. There are no significant differences as compared to using a Lorentzian model.
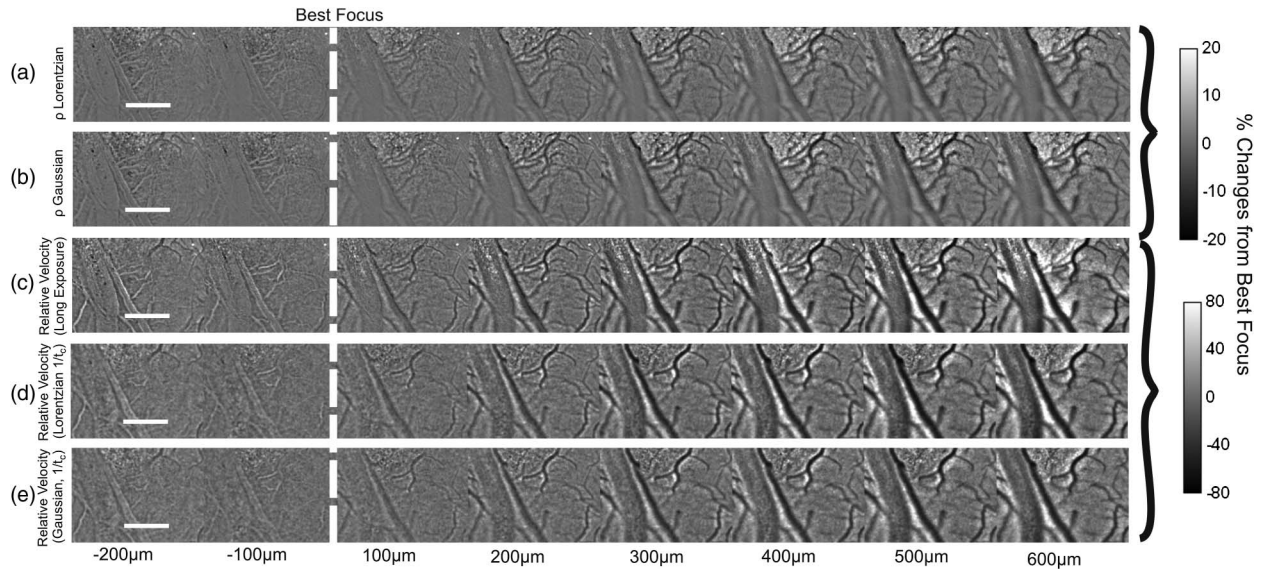
Fig. 4. (a), (b) Percentage changes of ρ for Lorentzian and Gaussian models from −200 to +600 μm. Changes of ±20% happen in vessels. (c)–(e) Percentage changes of relative velocity maps for long-exposure and Lorentzian/Gaussian models. Velocity measurements vary by as much as ±80% even when multi-exposure fitting is used.

with which high frequency components can be expected to defocus more rapidly as the focal plane is varied [19].

D. Depth Discrimination using Multiexposure

The results of Fig. 4 indicate that ρ can be estimated well even when imaging plane (i.e., focal plane) changes. We used this result to discern some information about vessel depth. As long as no major branches are seen along a vessel, a change in ρ implies a change in the proportion of static scatterers above and below the vessel, and we infer that vessel depth is changing. Measurements of deeper parts of the vessels will be subject to more static scatterers above, and as a result, from the definition of ρ, we can expect ρ to decrease. This has been verified using a green LED to find the best focus area and comparing to the values of ρ. By applying this principle along an individual vessel, we can use ρ as an indicator of vessel depth changes.

The changes of ρ along one vessel are shown in Fig. 5(a). The equation for ρ can be rearranged such that we find:

$$\gamma \equiv \frac{I_s}{I_f} = \left(\frac{1}{\rho} - 1 \right). \qquad (6)$$

The contribution from static scatterers I_s, above and below vessels depends on their concentration and volume, and we can specifically relate this to the type of tissue and depth. I_f, on the other hand, reflects the contribution from dynamic scatterers directly related to the blood flow velocity and vessel diameter, where the blood flow velocity is inversely proportional to the decorrelation time τ_c. Relative depth information was obtained by comparing values

of γ to best focus as estimated using a green LED [Fig. 5(b)]. We find correlation between γ and the relative depth information, suggesting that vessel depth is closely related to this new parameter. The large standard deviations are likely due to the inhomogeneous nature of tissue which this technique cannot account for. The concentration of static scatterers above the vessels is not constant throughout the whole wide-field image. However, if we presume that these concentrations have a small variance as compared to the variance in depths, we can expect to observe a correlation as in Fig. 5(b).

Obtaining a parameter well correlated to depth allows for the creation of a 3D map [Fig. 5(c)]. A mask of the in-focus vasculature is first overlaid to increase sharpness and to allow clear rendering of individual vessels. Making use of the linear fit [Fig. 5(b)], we translate γ into μm units. The relative depth values were obtained by taking the mean value of the five nearest neighbor pixels to reduce noise. Physiologically relevant observations can be made from this image. Small vessels from slightly deeper locations are observed to merge into a larger vein closer to the cortex, while velocity is found to increase with each joining branch. We sometimes notice dips/spikes in the relative depth measurements which are likely due to specular reflections, as opposed to scattering, off a vascular surface.

This 3D mapping technique is practical, as it can be obtained from images at a single focal plane. There is no need to move the camera focus up and down to obtain information about depth. However, because out of focus errors propagate strongly through this new parameter, depths of only about 200 μm can be resolved. This can, however, be improved by increasing the depth of field of the speckle contrast ratio map. Increasing the f-number will
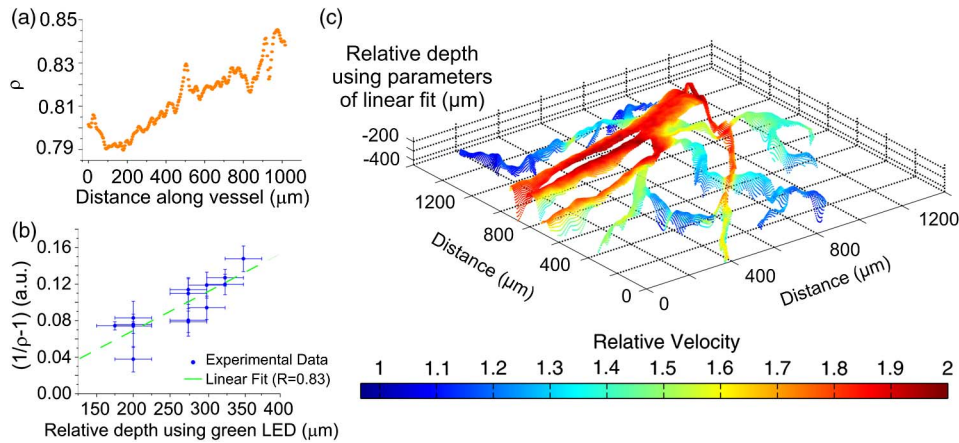
Fig. 5. (Color online) (a) Changes in ρ along a vessel with no major branching in/out suggests ρ can be used to estimate depth. (b) Comparing best focus using a green LED to $(1/\rho - 1)$ values. A correlation is observed which allows for estimation of vessel depth. (c) 3D map of in-focus vessels with depth estimated in microns using linear fit of (b). Color represents relative velocity as estimated from multiexposure data.

provide more in-focus data but will require increased illumination intensity, while decreasing magnification will lose small vessel features. However, due to the limited optical power of VCSELs, increasing f-number is not achievable at this point in time.

4. Discussion

In this paper, we have demonstrated the implementation of a multiexposure system adequate for portable imaging. Maps of ρ and relative velocity were obtained using the unique optical properties of VCSELs, limited by the camera frame rate and not by the transient times of the light source. The system uses the high dynamic range of the camera and the small changes in speckle contrast ratio of VCSEL currents, enabling exposures times spanning a factor of more than 600 times. However, the coherence length is altered with changes in the VCSEL current, changing speckle contrast ratio by not more than 15%. This change does not significantly affect maps of ρ and relative velocity. Acousto-optic systems [13,14] allow for a dynamic range which surpasses the one obtained by the presented method. Nevertheless, the dynamic range of our system is sufficient to provide accurate multiexposure data and to assess the errors associated with long-exposure speckle imaging. The technique detailed in this study allows the use of a small and simple system to obtain correct relative velocity maps in a portable implementation. Future work by our group includes performing multiexposure measurements using a CMOS camera (Genie HM 1400 XDR, Teledyne DALSA). Although CMOS cameras do not provide the same bit depth as CCD cameras, they can provide a similar exposure dynamic range that can be used in the portable regime. We see this compact system enabling imaging of relative velocity maps through thinned skull, thus minimizing the trauma to the animal for continuous and long-term measurements [14]. Furthermore, the use of VCSELs allows an easy integration of other techniques such as IOSI, creating a true

multimodality device [4,20]. We also envision the addition of fluorescence imaging as a third modality to increase the uses of the system, with the addition of a high-pass emission filter between the two lenses.

Accounting for static scatterers is extremely important, as it allows for more accurate relative flow maps, as demonstrated here with comparison to time-of-flight measurements (Fig. 3). This is important, as laser speckle imaging provides only relative values, and comparing flow from vein to artery could vary significantly from long- to multiexposure imaging. On the other hand, multiexposure is limited by the reduced frame rate at long-exposure times. Furthermore, the extra step of fitting to the equation at each pixel greatly impedes the potential of having a live view of relative flow maps, whereas the long-exposure technique can use a graphical processing unit for computation and live visualization [21]. In measurements where temporal changes are important, such as ischemia, the long-exposure technique is preferable due to its high frame rates. On the other hand, if a direct comparison of velocities between vessels is needed, an implementation accounting for the static scatterers is required for correct relative velocity maps. The multiexposure technique can also be easily implemented in long-term measurements due to its reduced frame rate.

Using multiexposure imaging provides additional information on the depth of a vessel, as estimated from the ratio of dynamic to total scatterers. Changes in height such as the ones observed during cortical swelling could potentially be detected using this technique. However, the relative depth maps are prone to errors due to the inhomogeneous nature of tissue and reflections off the surface of vessels. Furthermore, complications in surgery, such as cortical bruising, can prove costly in these depth measurements as they can have a strong effect on ρ. The current generation of VCSELs does not provide sufficient optical power for us to implement multiexposure measurements at high f-numbers that can

potentially increase the depth of field of the relative depth maps. At this time, depth data is estimated to within ± 200 μm of the focal plane. As compared to other depth scanning techniques, there is no need to move the camera plane while providing qualitative vessel topography estimates. As such, we see our technique as a powerful alternative in the portable animal brain imaging regime.

5. Conclusions

We have demonstrated a novel multiexposure method that enables measurements using the short transient times of VCSELs. We have also shown that our new compact system is adequate for correcting errors *in vivo* in long-exposure regimes and vessels with high velocity and static scatterers located above. Our results are in good agreement with other demonstrations done in microfluidic channels [13,14]. Making use of Gaussian or Lorenztian multiexposure models yielded no significant differences. This is due to the magnification used and the wide distribution of vessel size and velocity in our ROI. Using ρ in the multiexposure regime, extraction of depth information was possible and vasculature topography was inferred. Future work includes integration of the implementation into a portable system using a CMOS to monitor brain hemodynamics in a long-term study on freely-behaving animals.

References

1. P. Jones, H. Shin, D. Boas, B. Hyman, M. Moskowitz, C. Ayata, and A. Dunn, "Simultaneous multispectral reflectance imaging and laser speckle flowmetry of cerebral blood flow and oxygen metabolism in focal cerebral ischemia," J. Biomed. Opt. **13**, 044007 (2008).
2. Z. Luo, Z. Yuan, Y. Pan, and C. Du, "Simultaneous imaging of cortical hemodynamics and blood oxygenation change during cerebral ischemia using dual-wavelength laser speckle contrast imaging," Opt. Lett. **34**, 1480–1482 (2009).
3. A. Dunn, A. Devor, H. Bolay, M. Andermann, M. Moskowitz, A. Dale, and D. Boas, "Simultaneous imaging of total cerebral hemoglobin concentration, oxygenation, and blood flow during functional activation," Opt. Lett. **28**, 28–30 (2003).
4. H. Levy, D. Ringuette, and O. Levi, "Rapid monitoring of cerebral ischemia dynamics using laser-based optical imaging of blood oxygenation and flow," Biomed. Opt. Express **3**, 777–791 (2012).
5. A. Devor, I. Ulbert, A. Dunn, S. Narayanan, S. Jones, M. Andermann, D. Boas, and A. Dale, "Coupling of the cortical hemodynamic response to cortical and thalamic neuronal activity," Proc. Natl. Acad. Sci. USA **102**, 3822–3827 (2005).
6. F. Di Salle, E. Formisano, D. Linden, R. Goebel, S. Bonavita, A. Pepino, F. Smaltino, and G. Tedeschi, "Exploring brain function with magnetic resonance imaging," Eur. J. Radiol. **30**, 84–94 (1999).
7. K. Ghosh, L. Burns, E. Cocker, A. Nimmerjahn, Y. Ziv, A. El Gamal, and M. Schnitzer, "Miniaturized integration of a fluorescence microscope," Nat. Methods **8**, 871–878 (2011).
8. P. Miao, H. Lu, Q. Liu, Y. Li, and S. Tong, "Laser speckle contrast imaging of cerebral blood flow in freely moving animals," J. Biomed. Opt. **16**, 090502 (2011).
9. J. Goodman, "Some fundamental properties of speckle," J. Opt. Soc. Am. **66**, 1145–1150 (1976).
10. A. Fercher and J. Briers, "Flow visualization by means of single-exposure speckle photography," Opt. Commun. **37**, 326–330 (1981).
11. D. Boas and A. Dunn, "Laser speckle contrast imaging in biomedical optics," J. Biomed. Opt. **15**, 011109 (2010).
12. J. Ramirez-San-Juan, R. Ramos-García, I. Guizar-Iturbide, G. Martínez-Niconoff, and B. Choi, "Impact of velocity distribution assumption on simplified laser speckle imaging equation," Opt. Express **16**, 3197–3203 (2008).
13. A. Parthasarathy, W. Tom, A. Gopal, X. Zhang, and A. Dunn, "Robust flow measurement with multi-exposure speckle imaging," Opt. Express **16**, 1975–1989 (2008).
14. A. Parthasarathy, S. Kazmi, and A. Dunn, "Quantitative imaging of ischemic stroke through thinned skull in mice with multi-exposure speckle imaging," Biomed. Opt. Express **1**, 246–259 (2010).
15. M. Bouchard, B. Chen, S. Burgess, and E. Hillman, "Ultra-fast multispectral optical imaging of cortical oxygenation, blood flow, and intracellular calcium dynamics," Opt. Express **17**, 15670–15678 (2009).
16. R. Michalzik and K. Ebeling, *Vertical-Cavity Surface-Emitting Laser Devices* (Springer, 2002) p. 53.
17. Y. Atchia, H. Levy, and O. Levi, "Deviations in long exposure laser speckle contrast imaging: accounting for static scatterers," in *Applied Industrial Optics: Spectroscopy, Imaging and Metrology* (Optical Society of America, 2012).
18. D. Duncan, S. Kirkpatrick, and J. Gladish, "What is the proper statistical model for laser speckle flowmetry," Proc. SPIE **6855**, 685502 (2008).
19. E. Hecht, *Optics*, 4th ed. (Addison-Wesley, 2011) p. 552.
20. E. Munro, H. Levy, D. Ringuette, T. O'Sullivan, and O. Levi, "Multimodality optical neural imaging using coherence control of VCSELs," Opt. Express **19**, 10747–10761 (2011).
21. O. Yang, D. Cuccia, and B. Choi, "Real-time blood flow visualization using the graphics processing unit," J. Biomed. Opt. **16**, 016009 (2011).